# RANS modeling of scalar dispersion from localized sources within a simplified urban-area model

**By R. Rossi† S. Capra† AND G. Iaccarino**

## 1. Motivation and objectives

The use of RANS models in the analysis of the urban climate and in air quality studies has become increasingly popular when predictions have to deal with complex flows, such as those arising at the street-scale. The need for model assessment and validation has thus also become crucial towards establishing the reliability of RANS simulations of heat and mass transport in urban areas. In this research brief we evaluate RANS models for predicting dispersion from a localized source within the urban-canopy layer using a DNS database. The work is a follow-up of the DNS study of the same numerical experiment (Rossi & Iaccarino 2010), specifically designed to provide reliable concentration measurements and turbulence statistics for a simplified, but sufficiently challenging, urban-area model.

The work is focused towards a comparative study of anisotropic Algebraic Scalar Flux models (AFMs) versus the widespread, though isotropic, standard gradient-diffusion model (Rossi & Iaccarino 2009b). In the ongoing research project algebraic models have been successfully applied to the release of a contaminant in the wake of isolated obstacles (Rossi & Iaccarino 2009a; Rossi et al. 2010) as well as to the injection of a passive tracer in a separated flow over a wavy wall (Rossi 2010), showing improved accuracy over the standard model for the same flow and Reynolds stress predictions. In the present analysis we seek to complete the evaluation study of algebraic models for predicting dispersion in realistic urban-area models.

## 2. Flow setup

The flow setup employed in the computations is the single module case (1-MOD) explored in the DNS study (Rossi & Iaccarino 2010). The model consists of an $8 \times 8$ array of cubical obstacles, or buildings, of random height. The mean height of the buildings is $h_m$ and the random distribution is built upon a standard deviation of $0.3h_m$. The obstacles are arranged in a staggered fashion along the $x$ axis of the reference frame and the array is characterized by a packing-density $\lambda_p = NA_p/A_t$ of 25%, where $N$ is the number of obstacles, $A_p = h_m^2$ the obstacle area and $A_t$ the area of the computational domain. The scalar is emitted from a continuous volumetric source located in front of the tallest building and vertically displaced from the ground ($z_s/h_m = 0.2$). For the same source location, three different wind directions have been explored: $\alpha = 0°$, $\alpha = 45°$ and $\alpha = 90°$. The array geometry as well as the complex structure of the scalar plume developing downstream of the source are illustrated in Figure 1, depicting a snapshot from one of the DNS runs.

† Laboratorio di Termofluidodinamica Computazionale, Seconda Facoltà di Ingegneria di Forlì, Università degli Studi di Bologna, Via Fontanelle 40, 47100 Forlì, Italy

| case | $\Delta_w$ | $\Delta_1$ | $\Delta_2$ | $\Delta_3$ | $\Delta_4$ | $z_1/h_m$ | $z_2/h_m$ | $z_3/h_m$ | $z_4/h_m$ | $D_s/h_m$ | size |
|---|---|---|---|---|---|---|---|---|---|---|---|
| RANS | $h_m/32$ | $h_m/16$ | $h_m/8$ | $h_m/4$ | $h_m/2$ | 2.5 | 4 | 10 | 16 | 0.123 | 1.3M |
| DNS | $h_m/64$ | $h_m/32$ | $h_m/16$ | $h_m/8$ | - | 2.5 | 4 | 16 | - | 0.15 | 8M |

TABLE 1. Summary of grid spacing.

## 3. Numerical model

The RANS governing equations of the modeled passive and non-buoyant scalar plume can be written as follows:

$$\frac{\partial U_i}{\partial x_i} = 0 \tag{3.1}$$

$$\frac{\partial}{\partial x_j}(U_j U_i) = -\frac{1}{\rho}\frac{\partial P}{\partial x_i} + \nu\frac{\partial^2 U_i}{\partial x_j \partial x_j} - \frac{\partial}{\partial x_j}(\overline{u_i u_j}) + \Pi_i \tag{3.2}$$

$$\frac{\partial}{\partial x_j}(U_j C) = D\frac{\partial^2 C}{\partial x_j \partial x_j} - \frac{\partial}{\partial x_j}(\overline{u_j c}) + q_s, \tag{3.3}$$

where uppercase and lowercase characters denote mean and fluctuating values of flow variables. The $\Pi_i$ term represents the prescribed pressure-gradient driving the flow whereas $q_s$ is the scalar emission rate. The bulk Reynolds number $Re_b = U_e h_m/\nu$ of the flow, based on the mean velocity at the upper boundary of the flow domain $U_e$, lies in the range 7500 – 8000, depending on the flow angle, whereas the Schmidt number $Sc = \nu/D$ of the passive scalar field is 1. The flow is assumed to be fully developed, thus periodic conditions are enforced between the vertical boundaries of the computational domain, whereas at the same boundaries an outflow condition is applied for the scalar field.

The RANS computations are perfomed using the same grid topology as that employed for the DNS study, consisting of a hanging nodes-type hexahedral mesh using several levels of grid refinement from the upper boundary of the domain towards the cube array. A comparison of the grid resolution for the RANS and the DNS setup is shown in Table 1. As in the DNS case, the localized source is obtained by applying the source term $q_s$ at the right-hand side of Eq. (3.3) to a group of cells in which the centroid lies inside a sphere of radius $r/h_m = 0.05$. However, in the RANS setup the equivalent source size $D_s = (6\Delta V_s/\pi)^{1/3}$, where $\Delta V_s$ is the actual volume of the cell cluster, is slightly lower than in the DNS study owing to the coarser grid resolution (see Table 1). Further details about the flow setup and validation of DNS results can be found in Rossi & Iaccarino (2010).

## 4. Reynolds stress modeling

In order to provide a sufficient level of stress anisotropy to the algebraic flux models (Philips et al. 2010), the RANS momentum equation (3.2) is solved using a Reynolds-stress turbulence closure (Launder et al. 1975). For the present case, the transport equation for the Reynolds stresses $\overline{u_i u_j}$ can be written as follows:

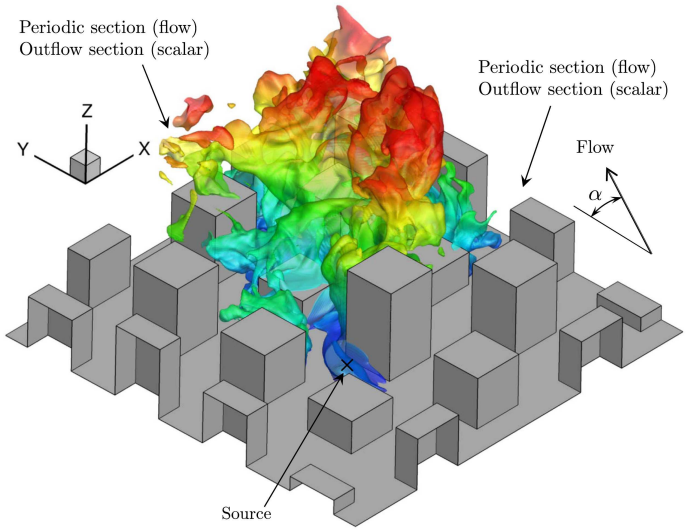


FIGURE 1. Sketch of flow setup and boundary condition for the present study.

$$\underbrace{\frac{\partial}{\partial x_k}(U_k\overline{u_iu_j})}_{C_{ij}\equiv\text{Convection}} = \underbrace{-\frac{\partial}{\partial x_k}\left[\overline{u_iu_ju_k}+\overline{\frac{p}{\rho}(\delta_{kj}u_i+\delta_{ik}u_j)}\right]}_{D_{T,ij}\equiv\text{Turbulent Diffusion}} + \underbrace{\frac{\partial}{\partial x_k}\left[\nu\frac{\partial}{\partial x_k}(\overline{u_iu_j})\right]}_{D_{L,ij}\equiv\text{Molecular Diffusion}}$$
$$\underbrace{-\left(\overline{u_iu_k}\frac{\partial U_j}{\partial x_k}+\overline{u_ju_k}\frac{\partial U_i}{\partial x_k}\right)}_{P_{ij}\equiv\text{Production}} + \underbrace{\overline{\frac{p}{\rho}\left(\frac{\partial u_i}{\partial x_j}+\frac{\partial u_j}{\partial x_i}\right)}}_{\phi_{ij}\equiv\text{Pressure Strain}} - \underbrace{2\nu\overline{\frac{\partial u_i}{\partial x_k}\frac{\partial u_j}{\partial x_k}}}_{\epsilon_{ij}\equiv\text{ Dissipation}}, \quad (4.1)$$

where $D_{T,ij}$, $\phi_{ij}$ and $\epsilon_{ij}$ are terms that need to be modeled.

The model for the pressure strain term $\phi_{ij} = \phi_{ij,1} + \phi_{ij,2} + \phi_{ij,w}$ is given by the linear formulation proposed by Gibson & Launder (1978), Fu et al. (1987) and Launder (1989). The slow and the rapid parts of $\phi_{ij}$ are modeled as

$$\phi_{ij,1} \equiv -C_1\frac{\epsilon}{k}\left[\overline{u_iu_j}-\frac{2}{3}\delta_{ij}k\right], \quad (4.2)$$

$$\phi_{ij,2} \equiv -C_2\left[(P_{ij}-C_{ij}-\frac{\delta_{ij}}{3}(P_{kk}-C_{kk})\right], \quad (4.3)$$

respectively. For the wall reflection term, which is responsible for the redistribution of normal stresses near the wall, the following model is adopted:

$$\phi_{ij,w} \equiv -C_1'\frac{\epsilon}{k}\left(\overline{u_ku_m}n_kn_m\delta_{ij}-\frac{3}{2}\overline{u_iu_k}n_jn_k-\frac{3}{2}\overline{u_ju_k}n_in_k\right)\frac{C_l k^{3/2}}{\epsilon d}$$
$$+C_2'\left(\phi_{km,2}n_kn_m\delta_{ij}-\frac{3}{2}\phi_{ik,2}n_jn_k-\frac{3}{2}\phi_{jk,2}n_in_k\right)\frac{C_l k^{3/2}}{\epsilon d}, \quad (4.4)$$

where $n_k$ is the $x_k$ component of the unit normal vector to the wall, $d$ is the wall normal

distance to the wall and $C_l = C_\mu^{3/4}/\kappa$, with $C_\mu = 0.09$ and $\kappa = 0.4187$ the Kármán constant.

The turbulent diffusion is modeled employing a scalar turbulent diffusivity (Lien & Leschziner 1994):

$$D_{T,ij} \equiv \frac{\partial}{\partial x_k}\left(\frac{\nu_t}{\sigma_k}\frac{\partial \overline{u_i u_j}}{\partial x_k}\right), \tag{4.5}$$

using $\sigma_k = 0.82$, whereas the dissipation tensor is modeled as

$$\epsilon_{ij} \equiv \frac{2}{3}\delta_{ij}\epsilon, \tag{4.6}$$

and the scalar dissipation rate obtained by solving an additional transport equation for $\epsilon$, which is not reported here for the sake of brevity. Note that the turbulent kinetic energy $k$ appearing in several of the modeled terms is obtained as the trace of the Reynolds stress tensor $\overline{u_i u_i}/2$.

The viscous affected region of the boundary layer is modeled using the one equation model of Wolfstein (1969):

$$\nu_t = C_\mu l_\mu \sqrt{k}, \tag{4.7}$$

where the turbulent viscosity is a function of the following length-scale:

$$l_\mu = y C_l \left(1 - e^{-Re_y/A_\mu}\right), \tag{4.8}$$

based on the turbulent Reynolds number $Re_y = y\sqrt{k}/\nu$ and the model constant $A_\mu = 70$. Note that the constants $C_1$, $C_2$, $C_1'$ and $C_2'$ in the pressure strain model are also modified close to the wall according to the model of Launder & Shima (1989) to account for low-Re effects.

Mean flow patterns at the base of the canopy, shown in Figure 2, have been found to be strongly influenced by incorporating the wall-reflection term (4.4) in the Reynolds stress model, eventually leading to a significant departure from the initial spread of the mean scalar plume near the source obtained from DNS statistics when wall reflection was not included.

## 5. Scalar flux modeling

### 5.1. *Standard gradient-diffusion hypothesis*

The simplest model for turbulent scalar fluxes follows from the Standard Gradient-Diffusion Hypothesis (SGDH), where the turbulent scalar flux is assumed to be proportional to the mean scalar gradient as follows:

$$\overline{u_j c} = -D_t \frac{\partial C}{\partial x_j}, \tag{5.1}$$

where $D_t = \nu_t/Sc_t$ is the eddy-diffusivity and $Sc_t$ denotes the turbulent Schmidt number. The customary value adopted for wall-bounded flows, $Sc_t = 0.9$, is employed in the computations and the eddy-viscosity provided by the Reynolds stress model adopted to compute the eddy-diffusivity. Note that away from the wall the eddy-viscosity is given

by the standard relationship $\nu_t = C_\mu k^2/\epsilon$, with $C_\mu = 0.09$, whereas Eq. (4.7) is employed in the viscous affected wall region.

### 5.2. *Algebraic flux models*

The algebraic models employed in the present work are formulated starting from the exact transport equation of the scalar fluxes $\overline{u_j c}$. For a non-buoyant fluid at high Reynolds numbers, the transport equation reads as follows:

$$\frac{D\overline{u_i c}}{Dt} = -\left(\overline{u_i u_l}\frac{\partial C}{\partial x_l} + \overline{u_l c}\frac{\partial U_i}{\partial x_l}\right) - (D+\nu)\overline{\frac{\partial c}{\partial x_l}\frac{\partial u_i}{\partial x_l}} + \overline{\frac{p}{\rho}\frac{\partial c}{\partial x_i}} - \frac{\partial}{\partial x_l}\left(\overline{u_l u_i c} + \frac{\overline{pc}}{\rho}\delta_{ij}\right). \tag{5.2}$$

The first and the second term on the right-hand side of Eq. (5.2) represent the scalar flux production and dissipation, the third one is the pressure-scalar-gradient correlation and the last term denotes the turbulent transport induced by velocity and pressure fluctuations. In the limit of homogeneous turbulence and further assuming a negligible contribution from convective transport, Eq. (5.2) simplifies as follows:

$$0 = \left(\overline{u_i u_j}\frac{\partial C}{\partial x_j} + \overline{u_j c}\frac{\partial U_i}{\partial x_j}\right) + \phi_{ic}, \tag{5.3}$$

where $\phi_{ic}$ represents the pressure-scalar-gradient correlation. The use of Eq. (5.3) is equivalent to invoking the hypothesis of *local-equilibrium* for the scalar fluxes, where the fluxes'growth rate due to the production term is limited by $\phi_{ic}$ only. In the framework of RANS computations, several modeling strategies for $\phi_{ic}$ have been proposed. However, these can always be expressed as a functional dependence of the following form:

$$\phi_{ic} = f\left(\overline{u_i c}, \frac{\partial U}{\partial x_j}, \frac{\partial C}{\partial x_j}\right), \tag{5.4}$$

leading to expressions which can be arranged as follows:

$$(\delta_{ij} - M_{ij})\overline{u_j c} = N_{ij}\frac{\partial C}{\partial x_j}, \tag{5.5}$$

where $M$'s and $N$'s are, in general, tensors consisting of the Reynolds stress tensor and the mean velocity gradient tensor.

An explicit algebraic expression for the scalar flux is obtained by inverting Eq. (5.5), which leads to the following expression for the scalar flux:

$$\overline{u_i c} = -C_c \tau_c k O_{ij}\frac{\partial C}{\partial x_j}, \tag{5.6}$$

where $k = \overline{u_i u_i}/2$ is the turbulent kinetic energy, $\tau_c$ is a characteristic time scale, $C_c$ is the model coefficient and the second-order tensor $O_{ij}$ is the tensorial eddy-diffusivity characterizing the algebraic model.

#### 5.2.1. *The generalized gradient-diffusion model*

The generalized gradient-diffusion model (GGDH) of Daly & Harlow (1970) represents one of the first attempts at developing a scalar flux model of the type (5.6). The tensorial

scalar diffusivity is simply assumed to be proportional to the Reynolds stress tensor, $O_{ij} = \overline{u_i u_j}/k$, leading to the following algebraic closure:

$$\overline{u_i c} = -C_c \tau_c \frac{\overline{u_i u_j}}{k} \frac{\partial C}{\partial x_j}. \tag{5.7}$$

The characteristic time scale in the GGDH model is assumed equal to that of the flow field, $k/\epsilon$, while the model coefficient extracted from simple shear experiments is $C_c = 0.3$.

5.2.2. *The high-order GGDH model*

The high-order generalized gradient-diffusion model (HOGGDH) developed by Abe & Suga (2001) seeks to improve the prediction of the streamwise scalar flux of the model of Daly and Harlow. In fact, if a simple-shear flow is considered, it is easy to show from Eq. (5.7) that the GGDH model yields $\overline{uc} \propto \overline{uv}$ and $\overline{vc} \propto \overline{v^2}$. However, in the wall-shear region scalar fluctuations are more correlated with $u$ than with $v$ for $Sc \geq 1$, thus $\overline{uc} \propto \overline{u^2}$, $\overline{vc} \propto \overline{uv}$ are expected to hold (Kim & Moin 1989). This is achieved in the high-order model by approximating the tensorial scalar diffusivity with the quadratic product of the Reynolds stress tensor, $O_{ij} = \overline{u_i u_k}\,\overline{u_k u_j}/k^2$. The HOGGDH model thus reads as follows:

$$\overline{u_i c} = -C_c \tau_c \frac{\overline{u_i u_k}\,\overline{u_k u_j}}{k^2} \frac{\partial C}{\partial x_j}. \tag{5.8}$$

As for the GGDH model, the time scale adopted in Eq. (5.8) is $k/\epsilon$, whereas the model coefficient obtained from simple shear experiments is $C_c = 0.575$.

## 6. Mean concentration metrics

The evaluation guidance protocol introduced by the Cost Action 732 - Quality Assurance and Improvement of Micro-Scale Meteorological Models (Schatzmann et al. 2010) is employed in the analysis of the scalar field to provide a comprehensive assessment of the RANS models as well as to limit the need for comparison of local mean concentration profiles. The metrics provided by the protocol are based on the normalized model results $P_i$ and the normalized observed or reference data $O_i$. In the present case, $P_i$ will represent the mean concentration coefficient $K$ predicted by the RANS model, whereas $O_i$ will be given by the coefficient computed from DNS data.

In the comparative study of the standard and algebraic flux models, the following metrics are employed:

- Hit rate ($q$):

$$q = \frac{1}{n}\sum_{i=1}^{n} N_i,\ N_i = \begin{cases} 1 & \text{for } \left|\dfrac{P_i - O_i}{O_i}\right| \leq F \text{ or } |P_i - O_i| \leq W \\ 0 & \text{else} \end{cases} \tag{6.1}$$

The hit rate provides the normalized fraction of predicted values within the allowed relative error threshold $F$ or within the allowed absolute error threshold $W$ over the total cell count $n$, where $F$ and $W$ are the relative uncertainty and repeatability of the reference dataset. A perfect model would yield $q = 1$.

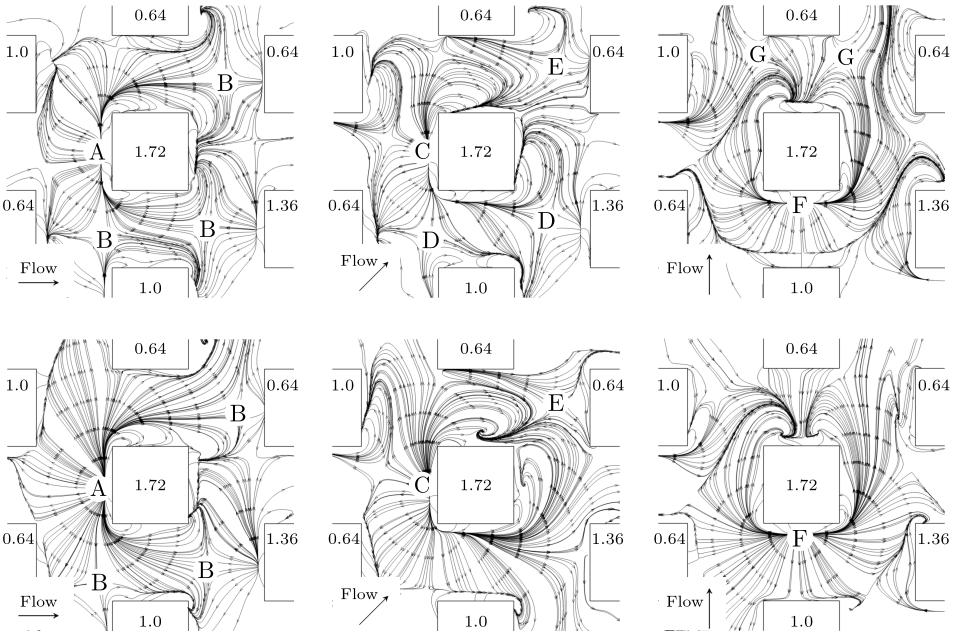


FIGURE 2. Numerical oil flow visualization of mean flow patterns at the base of the canopy. Top panels, DNS; bottom panels, RANS. The labels indicate the height of the elements relative to the mean height $h/h_m$.

- Geometric mean bias (MG):

$$\mathrm{MG} = \exp\left(\overline{\log O^*} - \overline{\log P^*}\right),\ O^* = \max\left(W, O_i\right),\ P^* = \max\left(W, P_i\right) \tag{6.2}$$

The geometric mean bias defined by Eq. (6.2), where the overbar denotes averaging over all data points, is applied separately to underpredicted and overpredicted mean concentration values from RANS models, leading to false-negative and false-positive indicators $M^-$ and $M^+$, respectively. The ratio $\mathrm{MG}^-/\mathrm{MG}^+$ is then employed to provide a measure of a systematic underprediction ($\mathrm{MG}^-/\mathrm{MG}^+ > 1$), or a systematic overprediction ($\mathrm{MG}^-/\mathrm{MG}^+ < 1$), characterizing the scalar flux model.

- Geometric variance (VG):

$$\mathrm{VG} = \exp[\overline{(\log O^* - \log P^*)^2}],\ O^* = \max(W, O),\ P^* = \max(W, P) \tag{6.3}$$

The geometric variance is employed to measure the amount of scatter in predicted values of mean concentration. As in the definition of the geometric mean bias, the overbar denotes averaging over all data points. The perfect model would again lead to $\mathrm{VG} = 1$.

The values suggested by Schatzmann et al. (2010) for the relative error threshold, $F$=0.25, are employed in the analysis, whereas the absolute error threshold is set to 10% of the maximum mean concentration observed in the DNS dataset. The concentration coefficient is given by $K = (CU_s h_m^2)/Q_s$, where $Q_s = q_s \Delta V_s$ is the scalar emission rate and $U_s$ the mean velocity magnitude at the source location.

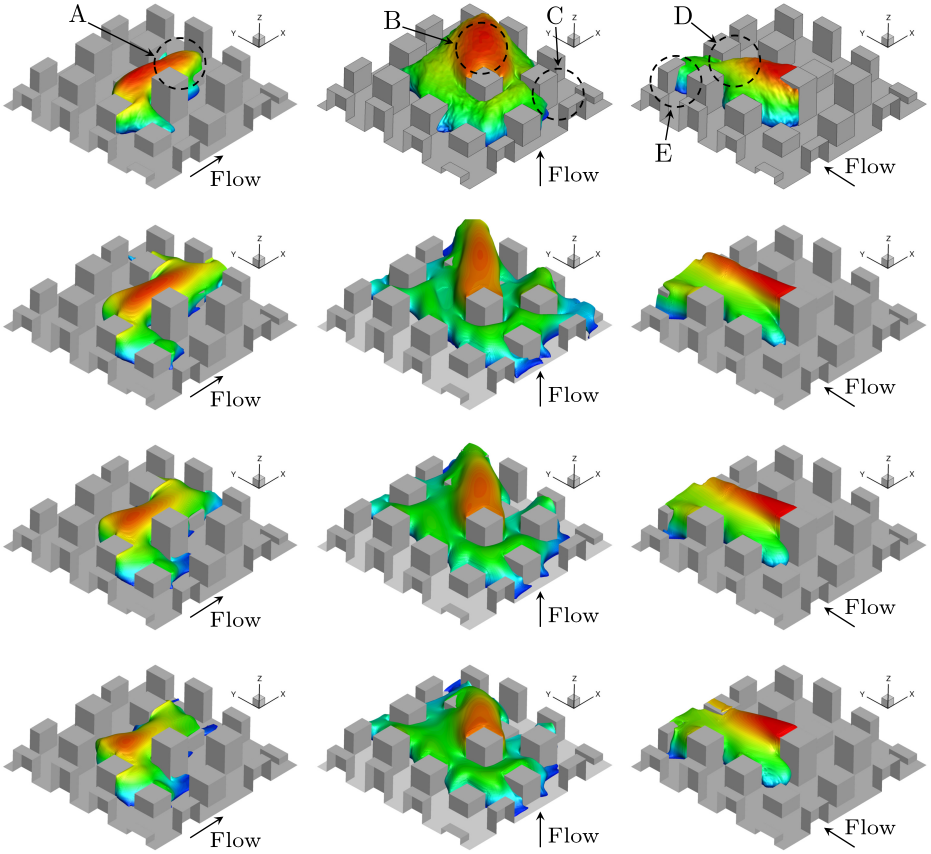


FIGURE 3. Iso-surfaces of concentration coefficient $K$. From top to bottom, DNS, SGDH, GGDH and HOGGDH; from left to right, $\alpha = 0^\circ$, $\alpha = 45^\circ$ and $\alpha = 90^\circ$.

## 7. Results and discussion

Discussion of results presented in this brief is limited to prediction of the mean concentration field. However, mean flow patterns at the base of the canopy are examined first to ensure that plume advection is similar in the DNS and in the RANS setup. Iso-surfaces of the mean concentration coefficient $K$ are presented next to provide a qualitative inspection of the estimated plume spread. The reliability of the standard and algebraic flux models is then evaluated with the help of scatter plots, which provide a one-by-one comparison with DNS data within selected regions downstream of the source, and quantified using the metrics introduced in the previous seciton.

### 7.1. *Mean flow patterns*

The mean flow patterns predicted by the Reynolds stress model are shown in Fig. 2 using oil flow-type visualizations obtained by projecting the velocity vector from the cell centroid adjacent to the wall to the ground. Since the scalar source is located close to the ground, the patterns induced by the three different wind angles have a strong impact on the initial spread of the plume and are thus examined first before moving to comparative study of the scalar flux models.

The patterns obtained for the case $\alpha = 0^\circ$ are clearly influenced by the staggered

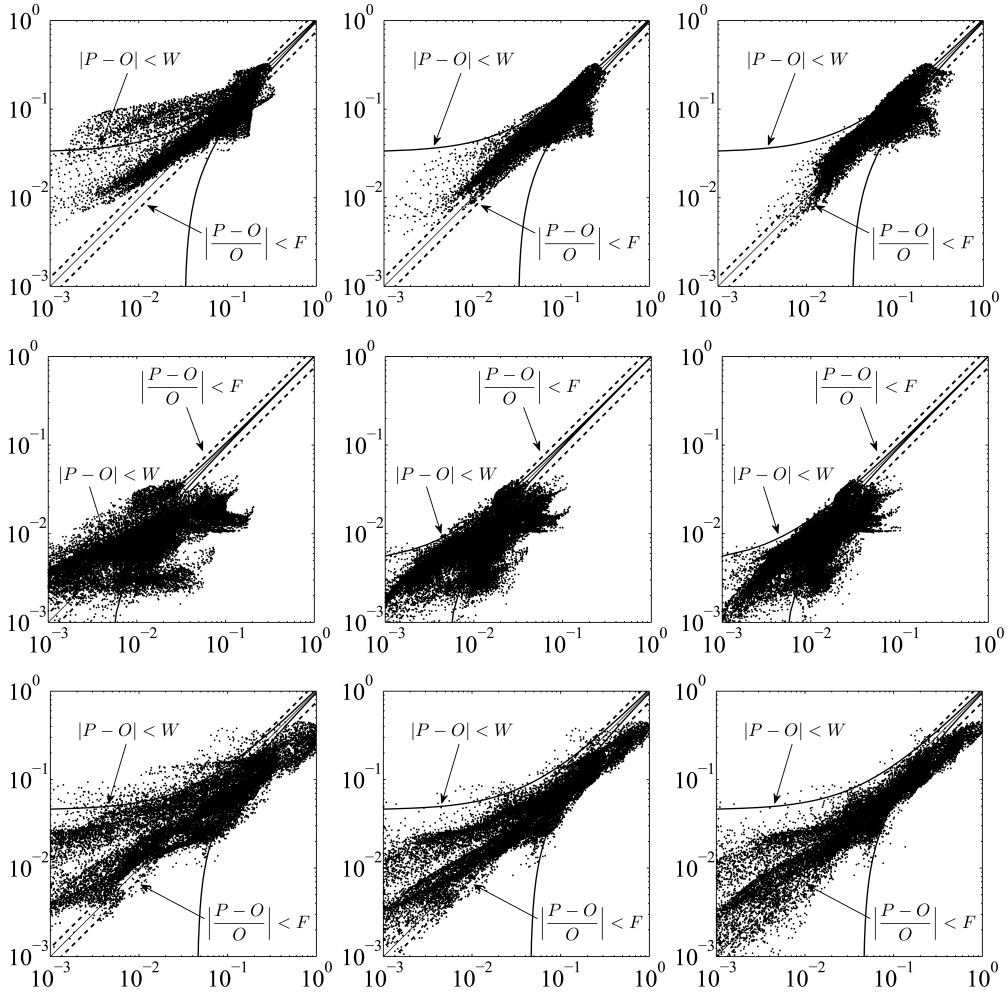


FIGURE 4. Scatter plots of the concentration coefficient $K$ predicted by RANS models ($x$ axis) versus DNS data ($y$ axis) within a bounding downstream of the scalar source. From left to right, SGDH, GGDH amd HOGGDH; from top to bottom, $\alpha = 0°$, $\alpha = 45°$ and $\alpha = 90°$.

arrangments of the array. In front of the tallest building the fingerprint of a horseshoe vortex (A) is clearly visible from both the DNS and RANS results. As the legs of this primary vortex extend and stretch out around the building, they eventually interfere with the downstream obstacles, leading to the formation of several saddle points (B) which are correctly predicted by the Reynolds stress model.

From the DNS results, the patterns induced by the skewed-flow regime $\alpha = 45°$ are found to be very similar to the staggered flow setup. However, only the saddle point arising in the wake of the tallest obstacle (E) is captured by the Reynolds stress model.

A similar issue appears in the aligned flow case $\alpha = 90°$, where only the nodal point in front of the tallest building (F) can be seen in both the DNS and RANS results. Nonetheless, since the mean flow proceeds around the buildings in a very similar fashion, the overall agreement between DNS and RANS results can be considered satisfactory in evaluating the scalar flux models.

| Flow angle | Model | $q$ | $\Delta q$ | $(MG^-/MG^+)$ | $\Delta(MG^-/MG^+)$ | VG | $\Delta$VG |
|---|---|---|---|---|---|---|---|
| $\alpha = 0^\circ$ | SGDH | 0.6262 | - | 1.7162 | - | 1.1423 | - |
| | GGDH | 0.8229 | +31.4% | 1.5548 | −9.4% | 1.0935 | −4.2% |
| | HOGGDH | 0.7994 | +27.6% | 1.5917 | −7.2% | 1.1010 | −3.6% |
| $\alpha = 45^\circ$ | SGDH | 0.4152 | - | 2.5323 | - | 1.74187 | - |
| | GGDH | 0.4145 | −0.2% | 2.1039 | −16.9% | 1.4592 | −16.2% |
| | HOGGDH | 0.5070 | +22.1% | 1.9283 | −23.8% | 1.3348 | −23.3% |
| $\alpha = 90^\circ$ | SGDH | 0.7443 | - | 1.7043 | - | 1.2075 | - |
| | GGDH | 0.7834 | +5.2% | 1.4238 | −16.4% | 1.1132 | −7.8% |
| | HOGGDH | 0.8251 | +10.8% | 1.3451 | −21.0% | 1.0833 | −10.2% |

TABLE 2. Computed metrics for the mean concentration field within a bounding box downstream of the scalar source.

### 7.2. *Mean scalar plume*

The iso-surfaces of the concentration coefficient shown in Figure 3 provides a preliminary insight into the different decay rate of mean concentration predicted by the scalar flux models. The overall picture given by the extension of the mean scalar plume is that of a systematic overprediction of the plume extent characterizing the standard flux model, in agreement with results observed for an isolated cubical obstacle (Rossi et al. 2010).

In the staggered flow case $\alpha = 0^\circ$, the extent of the plume in the streamwise direction (A) is found to be affected most by the algebraic GGDH and HOGGDH models, which are in better agreement with DNS data, whereas the lateral spread seems less influenced by the use of a tensorial diffusivity.

The streamwise development of the plume in the wake of the tallest building (B) in the oblique flow regime $\alpha = 45^\circ$ is also clearly affected by the scalar flow modeling. However, in this case the improvement provided by the algebraic models in the predicted lateral spread (C) is also significant.

A similar picture is found for the aligned flow case $\alpha = 90^\circ$, where both the region of the plume entrained in the wake of the building (D) and the subsequent spanwise development of the plume (E) benefit from the tensorial formulation of the eddy-diffusivity.

### 7.3. *Scatter plots and mean concentration metrics*

The scatter plots shown in Figure 4 compare the mean concentration coefficient $K$ predicted by RANS models ($x$ axis) to the observed DNS data ($y$ axis) within a bounding box located downstream of the source. The extent of each box is such as to wrap most of the volume of the scalar plume in the wake of the tallest building. The relative and the absolute error ranges adopted in the definition of the mean concentration metrics (6.1)-(6.3) are also shown in the plots as dashed and solid lines, respectively.

The improvement given by the algebraic models in predicting dispersion using the RANS equations is remarkable for each of the wind directions explored in the present study. The computed metrics within the same bounding box employed for the scatter plots and presented in Table 2 show an increase of the hit rate up to about 30% over the standard model and a reduction of about 20% in both the underprediction of the concentration coefficient and the scatter of computed values. Although the computed

values of the metrics depend upon the chosen size and location of the bounding box, it is also worth noting that the present results show a consistent improvement moving from the standard flux representation to algebraic models.

In the staggered flow regime the scatter plots show a major improvement in the mid to low range of the point cloud, where the SGDH model yields a significant departure from DNS statistics as well as a large amount of scatter in the data. The GGDH model is found to be the most accurate, although the concentration metrics characterizing the two algebraic formulations are similar.

High concentration values are found to be more sensitive to scalar flux models in the oblique flow case. The hit rate achieved by the RANS models is lower than that of the staggered flow regime, but the HOGGDH model again yields a significant improvement over the standard formulation. The GGDH model is also able to reduce the rate of underprediction and scattering by 15%, whereas the achieved hit rate is the same as that of the standard model for the present case.

The aligned flow case shows the highest hit rate, reaching almost 80% of the point cloud when the HOGGDH model is employed. The improvement over the standard formulation is twice as high compared to the GGDH model. The higher hit rate achieved in this case can be related to the channeled nature of the flow induced by the obstacles'alignment at $\alpha = 90^\circ$ (Rossi & Iaccarino 2010), which leads to Gaussian-like behavior of the scalar plume.

## 8. Summary and future work

In this research brief we presented a comparative study of scalar flux models for predicting dispersion in urban-like environments using the RANS equations. Algebraic models employing a tensorial diffusivity have been evaluated against the widespread standard diffusion model for the point release of a passive and buoyant-free scalar plume within a simplified urban-area model. Several wind directions, which lead to a different interaction of the plume with the underlying geometry, have been explored and the predicted values of mean concentration compared to a DNS database. In contrast to other similar studies (Izarra-Garcia et al. 2010), in the present analysis the scalar flux models have been evaluated starting from the same prediction of the mean velocity field and turbulent stresses, obtained by a Reynolds stress transport closure.

The impact of scalar flux models on the plume dispersion downstream of the source was remarkable. Algebraic models, and the high-order or quadratic formulation proposed by Abe & Suga (2001) in particular, provided a significant improvement over the standard scalar flux representation for any of the wind directions examined in the present study. Enhancement of predictive capabilities of RANS models has been quantified following the evaluation guidance protocol introduced in the work of Schatzmann et al. (2010), showing that the use of a tensorial diffusivity increases the hit count with respect to DNS data by 5% to 30%, depending on the flow angle. Available statistics from the DNS database for the three components of the scalar flux vector will be employed next to provide further insight into the reliability of the algebraic models.

## REFERENCES

Abe, K. & Suga, K. 2001 Toward the development of a Reynolds-averaged algebraic turbulent scalar flux model. *Int. J. Heat Fluid Flow* **22**, 19–29.

Daly, B. J. & Harlow, F. H. 1970 Transport equations in turbulence. *Phys. Fluids* **13**, 2634–2649.

Fu, S., Launder, B. E. & Leschziner, M. A. 1987 Modeling strongly swirling recirculating jet flow with Reynolds-stress transport closures. Sixth Symposium on Turbulent Shear Flows, Toulouse, France.

Gibson, M. M. & Launder, B. E. 1978 Ground effects on pressure fluctuations in the atmospheric boundary layer. *J. Fluid Mech.* **86**, 491–511.

Izarra-Garcia, R., Franke, J. & Franke, W. 2010 Pollution dispersion simulations of the MUST case using anisotropic turbulent scalar flux models. The Fifth International Symposium on Computational Wind Engineering, Chapel Hill, North Carolina, USA.

Launder, B. E. 1989 Second-moment closure and its use in modeling turbulent industrial flows. *Int. J. Num. Meth. Fl.* **9**, 963–985.

Launder, B. E. & Shima, N. 1989 Second-moment closure for the near-wall sublayer: development and application. *AIAA J.* **27**, 1319–1325.

Launder, B. E., Reece, G. J. & Rodi, W. 1975 Progess in the development of a Reynolds strees turbulence closure. *J. Fluid Mech.* **68**, 537–566.

Lien, F. S. & Leschziner, M. A. 1994 Assessment of turbulent transport models including non-linear RNG eddy-viscosity formulation and second-moment closure. *Comp. Fluids* **23**, 983–1004.

Kim, J. & Moin, P. Transport of passive scalars in a turbulent channel flow. In F. Durst (Ed.), Turbulent Shear Flows 6, Springer-Verlag, New York, 1989, pp. 85–96.

Philips, D. A., Rossi, R. & Iaccarino, G. 2010 The influence of normal stress anisotropy in predicting scalar dispersion with the $v^2 - f$ model. *Int. J. Heat Fluid Flow* **32**, 943–963.

Rossi, R. 2010 A numerical study of algebraic flux models for heat and mass transport in complex flows. *Int. J. Heat Mass Transf.* **53**, 4511–4524.

Rossi, R. & Iaccarino, G. 2009a Numerical simulation of scalar dispersion downstream of a square obstacle using gradient-transport type models. *Atmos. Environ.* **43**, 2518–2531.

Rossi, R. & Iaccarino, G. 2009b Computational aspects of scalar dispersion modeling and simulation in complex flows. *Nuovo Cimento Soc. Ital. Fis. C-Geophys. Space Phys.* **32**, 257–260.

Rossi, R. & Iaccarino, G. 2010 Scalar mixing from concentrated sources in urban-like roughness. *Annual Research Brief 2010, Center for Turbulence Research*, pp. 305–317.

Rossi, R., Philips, D. A. & Iaccarino, G. 2010 A numerical study of scalar dispersion downstream of a wall-mounted cube using direct simulations and algebraic flux models. *Int. J. Heat Fluid Flow* **31**, 805–819.

Schatzmann, M., Olesen, H. & Franke, J. 2010, COST 732 Model Evaluation Case Studies: Approach and Results. Technical Report 732, University of Hamburg.

Wolfstein, M. 1969 The velocity and temperature distribution of one-dimensional flow with turbulence augmentation and pressure gradient. *Int. J. Heat Mass Transf.* **12**, 301–318.